Mineralium Deposita (2002) 37: 452–464
DOI 10.1007/s00126-001-0247-2

ARTICLE

**Anne-Sylvie André-Mayer · Jacques Léon Leroy
Laurent Bailly · Alain Chauvet · Eric Marcoux
Luminita Grancea · Fernando Llosa · Juan Rosas**

Boiling and vertical mineralization zoning: a case study from the Apacheta low-sulfidation epithermal gold-silver deposit, southern Peru

Received: 28 May 2001 / Accepted: 31 October 2001 / Published online: 18 December 2001

Abstract The Au-Ag (±Pb-Zn) Apacheta deposit is located in the Shila district, 600 km southeast of Lima in the Cordillera Occidental of Arequipa Province, southern Peru. The vein mineralization is found in Early to Middle Miocene calc-alkaline lava flows and volcanic breccias. Both gangue and sulfide mineralization express a typical low-sulfidation system; assay data show element zoning with base metals enriched at depth and higher concentrations of precious metals in the upper part of the veins. Three main deposition stages are observed: (1) early pyrite and base-metal sulfides with minor electrum 1 and acanthite; (2) brecciation of this mineral assemblage and cross-cutting veinlets with subhedral quartz crystals, Mn-bearing calcite and rhombic adularia crystals; and finally (3) veinlets and geodal filling of an assemblage of tennantite/tetrahedrite + colorless sphalerite 2 + galena + chalcopyrite + electrum 2. Fluid inclusions in the mineralized veins display two distinct types: aqueous-carbonic liquid-rich Lw-c inclusions, and aqueous-carbonic vapor-rich Vw-c inclusions. Microthermometric data indicate that the ore minerals were deposited between 300 and 225 °C from relatively dilute hydrothermal fluids (0.6–3.4 wt% NaCl). The physical and chemical characteristics of the hydrothermal fluids show a vertical evolution, with in particular a drop in temperature and a loss of H_2S. The presence of adularia and platy calcite and of co-existing liquid-rich and vapor-rich inclusions in the ore-stage indicates a boiling event. Strong H_2S enrichment in the Vw-c inclusions observed at –200 m, the abundance of platy calcite, and the occurrence of hydrothermal breccia at this level may indicate a zone of intense boiling. The vertical element zoning observed in the Apacheta deposit thus seems to be directly related to the vertical evolution of hydrothermal-fluid characteristics. Precious-metal deposition mainly occurred above the 200-m level below the present-day surface, in response to a liquid/vapor phase separation due to an upward boiling front.

Keywords Epithermal gold-silver · Peru · Andes · Boiling

Editorial responsibility: O. Christensen

A.-S. André-Mayer (✉) · J.L. Leroy · L. Grancea
UMR Géologie et Ressources Minérales et Energétiques,
Université Henri Poincaré, B.P. 239,
54506 Vandoeuvre-lès-Nancy Cedex, France
E-mail: anne-sylvie.andre@g2r.uhp-nancy.fr

L. Bailly
BRGM, REM/MESY, Avenue Claude Guillemin,
B.P. 6009, 45060 Orléans Cedex 2, France

A. Chauvet
ISTO, FRE 2124, Université d'Orléans,
Bât. Géosciences, B.P. 6759,
45067 Orléans Cedex 2, France

E. Marcoux
ISTO, Université d'Orléans,
8 rue Léonard de Vinci,
45072 Orléans Cedex 2, France

F. Llosa · J. Rosas
Cedimin S.A., Luis Saenz 447–449 Jesus Maria,
Lima 21, Peru

Introduction

Hydrothermal processes linked to mineralization and alteration are relatively well understood in epithermal deposits, especially in the low-sulfidation type which formed in a similar environment to that of active geothermal systems (Henley and Ellis 1983). Numerous papers dealing with this type of deposit are well compiled in Hedenquist's (1996) review volume. In spite of their various volcanic and tectonic settings, a general scheme has been proposed and recognized in many low-sulfidation epithermal deposits (Buchanan 1981; Berger and Eimon 1983; Silberman and Berger 1985; Clarke and Govett 1990; Pirajno 1992; Sherlock et al. 1995). A zoning between base- and precious metals is recognized in both low-sulfidation epithermal deposits and geothermal

areas, with precious-metal mineralization tending to be more abundant in the upper part of the deposits (Ewers and Keays 1977; Hedenquist and Henley 1985a; Hollister and Silberman 1995; Simmons and Browne 2000).

The Arequipa-Orcopampa area is located about 600 km southeast of Lima in the Cordillera Occidental of southern Peru (Fig. 1). Several base- and precious-metal epithermal deposits in Neogene volcanic rocks, such as Arcata, Cailloma, Madrigal, Suyckutambo, Orcopampa, and Shila, characterize this region (Fig. 1). The overall mineralogy of these deposits is consistent with low-sulfidation epithermal mineralization, except for the Chipmo area (Orcopampa district) where veins of the high-sulfidation epithermal type were recognized by Jannas (1998). Vertical and lateral zoning of Pb, Sb, Cu, As, and Ag concentrations and of the base to precious-metal ratio have been described from the Orcopampa (Gibson et al. 1990; Petersen et al. 1990) and Arcata mines (Candiotti et al. 1990).

Mine-assay data from the Shila veins show a general base-metal enrichment at depth and higher concentrations of precious metals in the upper parts. A detailed

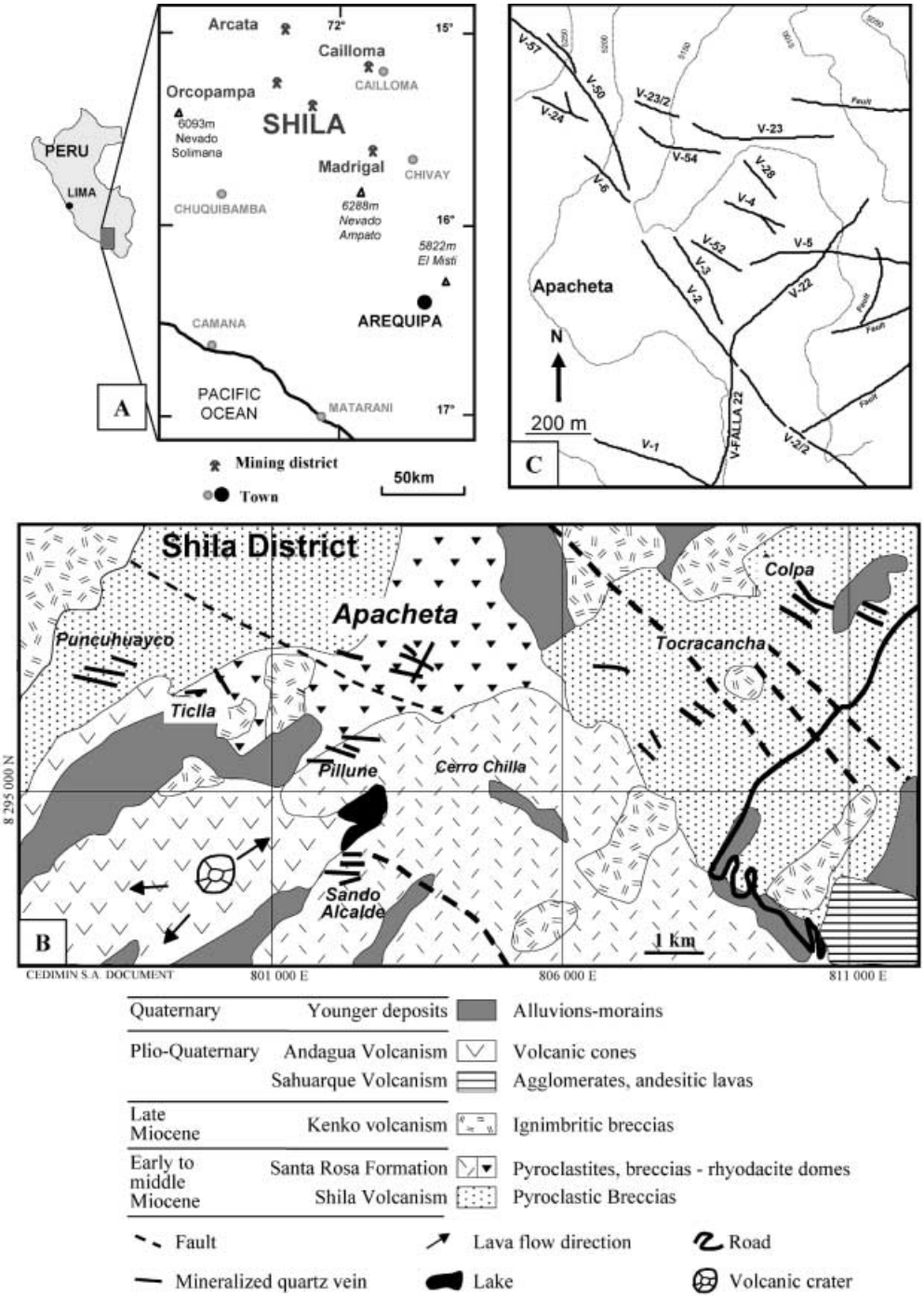

Fig. 1 **A** Geographic position of the epithermal district of Shila. **B** Geologic map of the Shila district with location of the main deposits (modified from a Cedimin S.A. document). **C** Location and orientation of the different mineralized veins of the Apacheta deposit

mineralogical and fluid-inclusion study was thus carried out on the Apacheta vein system in the Shila district, to document and study this vertical zoning and to explain why economic mineralization is limited to the uppermost 200 m below the present-day erosion surface.

Geological setting

The Shila-Apacheta vein system is part of the Shila-Paula district hosted by Neogene volcanic rocks (Fig. 1). The area is underlain by a folded sedimentary basement, comprising Jurassic sandstone, shale and limestone of the Yura Group, and Cretaceous limestone (Murco and Arcurquina Formations), unconformably overlain and/or intruded by a complex unit of Neogene volcanic rocks. Precious-metal ores are found within Early to Middle Miocene calc-alkaline volcanic rocks that include lava flows and volcanic breccia. The Shila district, which went into production in 1990, includes the Apacheta, Pillune, Sando Alcalde, Puncuhuayco, Ticlla, Tocracancha, and Colpa deposits, each consisting of several mineralized veins (Fig. 1). Only Apacheta, Pillune, and Sando Alcalde have been mined so far.

The mineralized veins generally trend E–W (Pillune, Sando Alcalde, Ticlla, Puncuhuayco), NW–SE (Apacheta, Colpa, Tocracancha), and exceptionally NE–SW (Apacheta, Puncuhuayco) (Chauvet et al. 1999; Cassard et al. 2000). They are generally thin (0.2–2.5 m), steeply dipping ($>75°$) to the north or south, and about 100 m long and 150–200 m high. Cassard et al. (2000) published K/Ar radiometric measurements on host rocks and veins, giving ages of 10.94 ± 0.13 and 10.56 ± 0.12 Ma for Sando Alcalde and Pillune, respectively (Table 1). The Shila district appears to be about 5–7 Ma younger than the neighboring Orcopampa (Gibson et al. 1995) and Cailloma (Silberman et al. 1985) vein systems, and is similar in age to the Suyckutambo deposit (Petersen et al. 1983). The Shila gold-bearing veins and especially the veins of the Sando Alcalde and Pillune areas show a systematic association between first-order structures, mainly E–W to ENE–WSW oriented, and second-order ones trending NE–SW. Chauvet et al. (1999) and Cassard et al. (2000) recently proposed a two-stage tectonic model: the first event was a left-lateral shearing from the effects of NE- to SW-trending horizontal compression, the second one being a re-opening of the previously formed structures under the effects of a N120°E-oriented tectonic force. At this stage, it is difficult to definitively integrate the Apacheta system, with its different vein orientations, into this general structural model.

Table 1 K/Ar age determinations of volcanic rocks from the Shila area. (Modified from Cassard et al. 2000)

Deposit – rock/vein	Material	K/Ar ages ($Ma \pm 1\sigma$)
Pillune – vein 21	Adularia	10.56 ± 0.12
Sando Alcalde – vein 74	Adularia	10.94 ± 0.13
Dacitic flow	Whole rock	13.0 ± 0.6
Dacitic flow	Whole rock	12.9 ± 0.6

Mineralogy

Mineralized samples from different veins and levels of the Apacheta vein system (Table 2) were examined in order to reconstruct the paragenetic succession. Three main deposition stages are observed in each vein (Fig. 2):

Stage 1

The earliest sulfide mineral is invariably pyrite, with extensively fractured sub-euhedral crystals that are locally replaced by other base-metal sulfides (Fig. 3A). This pyrite is followed by light-yellow sphalerite-1 crystals (Fig. 3D), characterized by low to moderate Fe (0.34–1.70 wt%), Mn (0–0.37 wt%), and Cd (0.51–1.58 wt%) contents. Galena commonly occurs as inclusions in pyrite and as large independent crystals, and acanthite is also observed as inclusions in pyrite. Scarce electrum-1 grains with an Au content of 62.9–71.6 wt% (Fig. 4) occur as inclusions in pyrite (Fig. 3B), and more rarely in sphalerite 1 and as free grains in gangue quartz.

Stage 2

The stage-1 mineralogical assemblage is crosscut and brecciated by veinlets containing subhedral quartz

Table 2 Structural position of studied samples from the Apacheta deposit. *Italics* indicates samples on which fluid-inclusion studies were conducted

Altitude (m)	Depth (m)	Veta 1	Veta 2	Veta 5	Veta 22	Veta 50	Veta 51	Veta 54	Veta 57
5,250	0		SHA 10						SHA 29
5,220	–30	*SHA 3*							
5,150	–100		SA 30, 32		SA 33		*SHA 30*		
5,100	–150		SHA 25			SHA 26			
5,050	–200			*SHA 12*	SA 35	SHA 20, 21		SHA 22, 31	
5,020	–230		*SA 40*						
5,000	–250				*SHA 28*				
4,975	–275		SHA 23, 24						

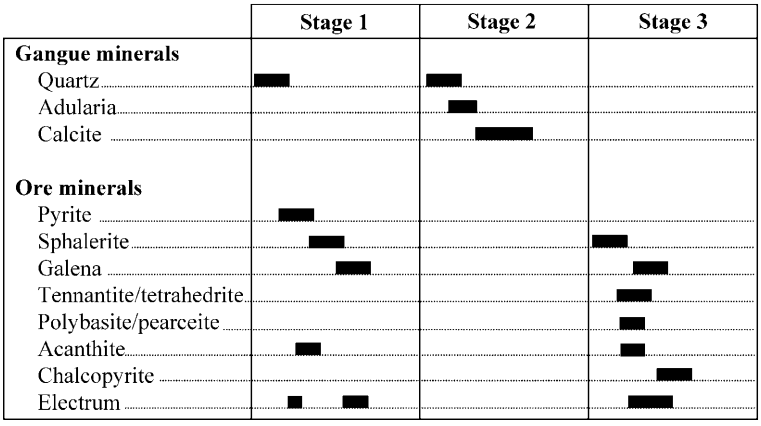

Fig. 2 Generalized paragenetic sequence of the different veins in the Apacheta area

crystals, Mn-bearing calcite, and rhombic adularia crystals. Quartz dominates in the higher part of the vein, whereas calcite – commonly presenting a bladed habit (Fig. 3C) – occurs in the deeper part of the mineralized zone.

Stage 3

Sulfide deposition continued with the precipitation as veinlets and geodal fillings of a tennantite/tetrahedrite + colorless sphalerite 2 + galena + chalcopyrite + electrum 2 assemblage (Fig. 3E, F). Myrmekitic textures between tennantite/tetrahedrite and galena as well as between galena and chalcopyrite are common. Tetrahedrite shows variable Ag content, in places reaching over 17 wt%. The same range of tennantite/tetrahedrite composition is observed regardless of the vertical location of the sample. Iron content in sphalerite 2 is rarely significant and consistently below 0.6 wt%. Grains of electrum 2 with an Au content of 72–81 wt% appear as inclusions in tennantite/tetrahedrite, in galena, and more rarely in chalcopyrite (Fig. 4). Above level 5,150 m up to the surface, tennantite/tetrahedrite coexist with polybasite/pearceite, partially replaced by acanthite. The scarce electrum grains in polybasite/pearceite have a gold content of 46–56 wt% (Fig. 4).

Average Au/Ag ratios for each level (whole rock analyses) increase toward the surface (Fig. 5), essentially through an increase in Ag. All veins of the Apacheta system show the same mineralogical assemblage, with the same chemical composition and paragenetic succession, suggesting similar and contemporaneous depositional processes.

Fluid-inclusion studies

In order to reconstruct the physico-chemical evolution of the hydrothermal fluids from stage 1 to stage 3, and from bottom to top of the mineralized columns, a fluid-inclusion study was conducted on mineralized samples taken from different veins (Table 2) and at depths of –250 m (SHA 28), –230 m (SA 40), –200 m (SHA 12), –150 m (SHA 30), and –30 m (SHA 3). The studied fluid inclusions are hosted by light-yellow sphalerite 1 (stage 1), quartz and calcite (stage 2), and colorless sphalerite 2 (stage 3) from mineralized veins and also in quartz phenocrysts of the host rock adjacent to the veins. The studies consisted of microscopic, microthermometric, and Raman-spectroscopic observations, and were done on thick wafers using a Chaixmeca heating–freezing stage (Poty et al. 1976). The stage was calibrated with melting-point standards at $T > 25$ °C and natural and synthetic fluid inclusions at $T < 0$ °C. Salinity expressed in wt% NaCl was calculated from microthermometric data using equations from Bodnar (1993). The presence and molar fraction of gas (CO_2, H_2S, N_2) were determined in individual fluid inclusions by Raman analyses on a Dilor X-Y multi-channel modular Raman spectrometer (Dubessy et al. 1984).

Petrography of fluid inclusions

The fluid inclusions analyzed were either primary or secondary in origin, using the criteria of Roedder (1984) and Bodnar et al. (1985). Two fluid-inclusion types are identified at room temperature and include (Fig. 6), using the convention of Boiron et al. (1992):

- Aqueous-carbonic liquid-rich inclusions (Lw-c; w for water; c for carbonic) commonly with 10–20 vol% vapor phase are observed as primary and secondary inclusions in sphalerite 1, quartz and calcite of stage 2, and sphalerite 2, and as secondary-plane inclusions in host-rock quartz. The size of these inclusions ranges from 3–200 μm with a majority between 10 and 20 μm.
- Aqueous-carbonic vapor-rich (Vw-c) fluid inclusions with more than 90 vol% vapor phase and a small rim of liquid water occur as primary and mainly as secondary inclusions in the stage-2 ore-vein quartz and always as secondary-plane inclusions in the host-rock

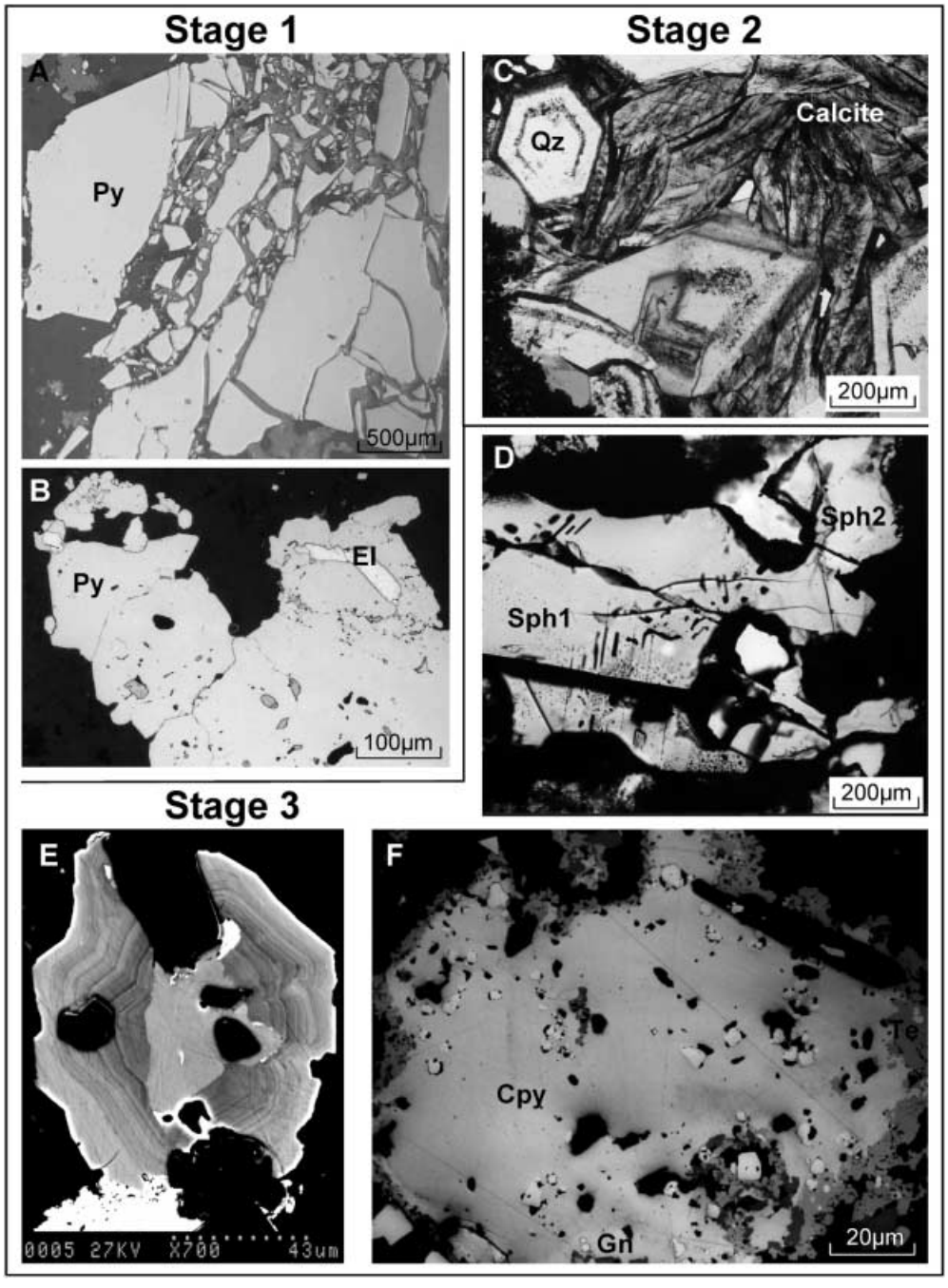

Fig. 3A–F Photomicrographs showing the three stages of mineralization with typical ore and gangue mineral assemblages. **A** Early fractured pyrite (*Py*); **B** inclusions of electrum (*El*) in pyrite; **C** gangue assemblage of stage 2 with subhedral quartz (*Qz*) and platy calcite; **D** light-yellow sphalerite crystals – sphalerite 1 (*Sph1*), stage 1 – and colorless sphalerite – sphalerite 2 (*Sph2*), stage 3; **E** zoned tennantite (*dark part*) and tetrahedrite (*clear part*); **F** main mineral assemblage of stage 3 with a geodal filling of tennantite-tetrahedrite, galena (*Gn*), and chalcopyrite (*Cpy*). **A**, **B**, and **F** were taken in reflected light, **C** and **D** in transmitted light; **E** is an SEM backscatter image

quartz. In some rare inclusion planes, the vapor phase is highly variable, from 10–100 vol% vapor. The size of these inclusions is constant between 3 and 30 µm.

Microthermometric and Raman results

Microthermometric and Raman studies were conducted on these various types of fluids, and the main results are presented in Tables 3, 4 and Figs. 7 and 8.

Aqueous-carbonic liquid-rich fluids (Lw-c)

Primary inclusions in sphalerite 1 show melting temperatures of ice (Tm_{ice}) ranging from –4.0 to –6.3 °C (6.4–9.5 wt% NaCl), with homogenization temperatures (Th) in the liquid field ranging from 258–271 °C. The secondary inclusions in the same sphalerite 1 show lower salinity (3.4–1.6 wt% NaCl) for similar Th (248–270 °C).

In quartz and calcite of stage 2, the Lw-c fluids have a Tm_{ice} from –0.1 to –1.6 °C (0.2–2.6 wt% NaCl) and Th, always to the liquid phase, ranging from 224–299 °C.

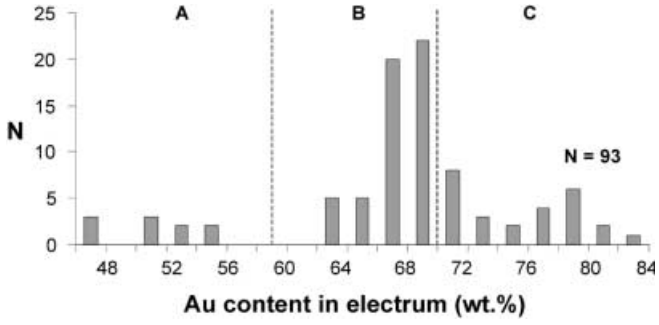

Fig. 4A–C Distribution of Au content of electrum in vein 2 (wt%, electron microprobe analyses). **A** Electrum grains included in polybasite/pearceite above level 5,150 m; **B** electrum grains associated with stage 1 base-metal sulfides; **C** electrum grains associated with stage 3 base- and silver-metal sulfides. *N* Number of measurements

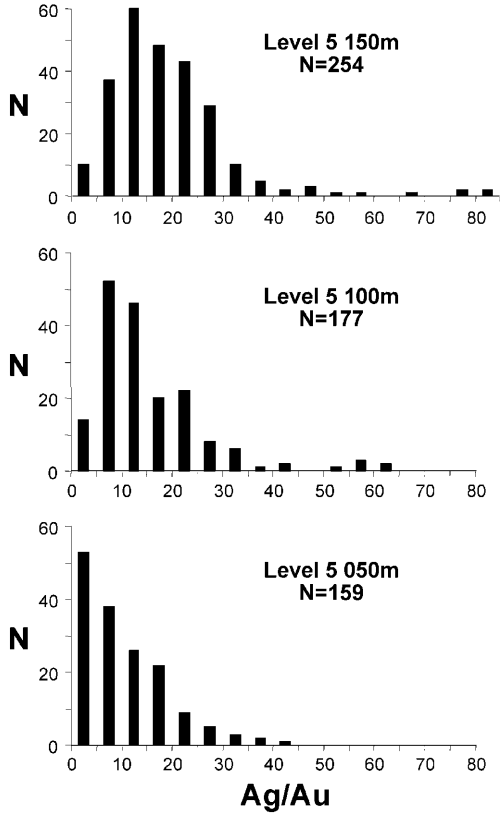

Fig. 5 Vertical evolution of the Ag/Au ratio in vein 2 between levels 5,150 and 5,050 m (whole-rock analyses). *N* Number of measurements

Slight differences exist between the primary and secondary inclusions (Tables 3, 4), the latter generally having a lower salinity than the former, for similar Th from samples at the same structural level. The low eutectic temperature (<-30 °C) indicates the presence of bivalent cations. Presence of minor CO_2 in the gaseous phase was detected by Raman spectroscopy, but with a too low concentration to be quantified. No clathrate formation and melting were observed during microthermometric tests.

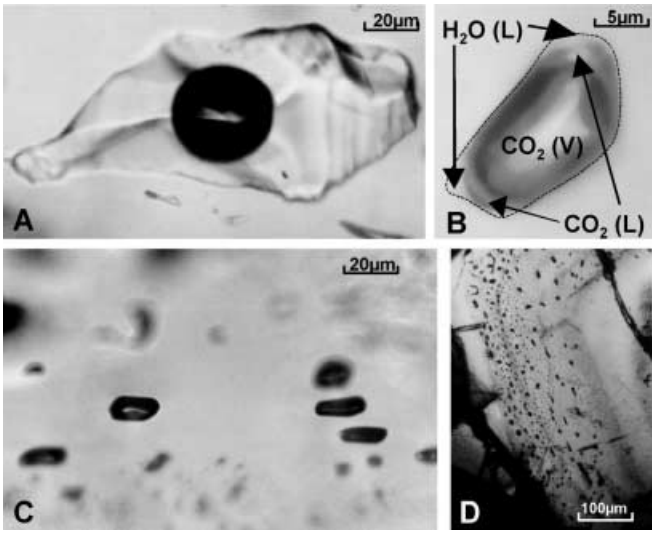

Fig. 6A–D Photomicrographs of the different fluid types observed in the Apacheta deposit. **A** Aqueous-carbonic liquid-rich inclusion in quartz (Lw-c); **B** aqueous-carbonic vapor-rich inclusion (Vw-c): *L* liquid; *V* vapor; **C** homogeneous fluid-inclusion planes of Vw-c fluid; **D** primary fluid inclusions in sphalerite 1

Primary fluid inclusions in sphalerite 2 have salinity (0.6–0.9 wt% NaCl) and Th (275–285 °C) values that are similar to those of the secondary inclusions in quartz and calcite 2 for the same structural level.

Aqueous-carbonic vapor-rich fluids (Vw-c)

Microthermometric investigation of vapor-rich fluid inclusions was hindered by the small volume of the liquid phase. Thus, freezing and heating experiments were restricted to larger inclusions with good optical properties. The Vw-c inclusions show Tm_{CO_2} ranging from –57.9 to –59.3 °C. Rare Th_{CO_2} values, between –1.3 and +6.5 °C (in vapor phase), indicate a low fluid density. The clathrate fusion temperatures range from –4.3 to +6.5 °C. Gas analyses show CO_2 (62.9–100 mol%) with less N_2 (0–37.1 mol%) and H_2S (0.7–6.7 mol%) (Fig. 8). The rare Th values, always to the vapor phase, are between 250 and 300 °C. No differences were noted between primary and secondary inclusions in vein quartz, and for secondary inclusions in quartz from the host rock.

Temporal and vertical evolution of physico-chemical fluid characteristics

Constraints from Lw-c fluids

A clear decrease in both salinity and homogenization temperature is observed from stage 1 (sphalerite 1) to stage 3 (sphalerite 2). Microthermometric data on primary Lw-c fluid inclusions trapped in stage-2 quartz

Table 3 Microthermometric data for fluids observed in the Apacheta deposit. *Abbreviations* for the different microthermometric parameters are defined in the text. *n* Number of measurements

Inclusion type	Sample (level, actual depth)	Mineral		Tm_{ice} (°C) *(n)*	Th (°C) *(n)*	Salinity (wt% NaCl)	Tm_{CO_2} (°C) *(n)*	Th_{CO_2} (°C) *(n)*	Tf_c (°C) *(n)*
Lw-c	SHA 3 (5,220 m, –30 m)	Quartz calcite	Primary	–0.3 to 0.9 *(42)*	224–243 *(42)*	0.5–1.6	–	–	–
			Secondary	–0.1 to 0.6 *(66)*	220–239 *(59)*	0.2–1.0	–	–	–
	SHA 12 (5,050 m, –200 m)	Sphalerite 1	Primary	–4.0 to –6.3 *(13)*	254–271 *(10)*	6.4–9.5	–	–	–
			Secondary	–0.9 to –2.0 *(29)*	248–270 *(25)*	1.6–3.4	–	–	–
		Quartz calcite	Primary	–0.4 to 1.5 *(33)*	234–275 *(28)*	0.7–2.6	–	–	–
			Secondary	–0.1 to 0.8 *(47)*	246–275 *(39)*	0.2–1.4	–	–	–
	SA 40 (5,020 m, –230 m)	Sphalerite 2	Primary	–0.3 to –0.5 *(5)*	275–285 *(5)*	0.6–0.9	–	–	–
	SHA 28 (5,000 m, –250 m)	Quartz calcite	Primary	–0.6 to –1.4 *(29)*	260–299 *(24)*	1.0–2.4	–	–	–
			Secondary	–0.3 to –0.8 *(50)*	255–290 *(47)*	0.5–1.4	–	–	–
Vw-c	All levels	Qz	Primary Secondary	–	250–300 *(37)*	–	–57.9 to –59.3 *(20)*	–1.3 to +6.5 *(15)*	–4.3 to +6.5 *(7)*

Table 4 Raman data for fluids observed in the Apacheta deposit. *Qz* quartz

Inclusion type	Sample (level, actual depth)	Mineral	CO_2 (mol%)	H_2S (mol%)	N_2 (mol%)
Vw-c	SHA 3 (5,220 m, –30 m)	Qz	100	–	–
			100	–	–
			100	–	–
			100	–	–
	SHA 12 (5,050 m, –200 m)	Qz	97.7	1.3	1.0
			77.5	20.5	2.0
			95.1	4.0	0.9
			85.5	7.8	6.7
			88.9	7.8	3.3
			95.7	3.6	0.7
			79.4	15.3	5.3
			84.3	10.9	4.8
	SHA 28 (5,000 m, –250 m)	Qz	72.0	27.1	0.9
			62.9	37.1	–
			65.3	33.9	0.8
			69.9	31.1	–

plotted against depth (Fig. 9) show a decrease of the homogenization temperature from the deepest sample (SHA 28, –250 m actual depth; average Th: 290 °C) to the highest sample (SHA 3, –50 m actual depth; average Th: 235 °C).

The average salinity value of 2.1 wt% NaCl is similar for all vertical profiles (Fig. 7), and is comparable to those described for gold–silver-dominated epithermal systems (Hedenquist and Henley 1985a). The exception are primary inclusions in sphalerite (SHA 12), even if the presence of trace CO_2, detected by Raman spectroscopy, can contribute to the final ice melting and thus may slightly increase the apparent salinity of the inclusions (Bozzo et al. 1973; Collins 1979; Ramboz 1980; Hedenquist and Henley 1985b).

Constraints from Vw-c fluids

Raman-microprobe analyses of the volatile phase of Vw-c inclusions in homogeneous planes with more than 90 vol% of vapor indicate that CO_2 is the dominant component (> 72 mol% of the vapor phase) and is present throughout the profile (Fig. 8). N_2 content decreases upward from more than 20 mol% of the vapor phase at depth to 0 mol% in the upper part of the system. H_2S, only detected as traces at –250 m, is very well expressed at –200 m where it can represent more than 6 mol% of the vapor phase. The molar CO_2/H_2S ratio, controlled by a matrix of redox equilibria (Giggenbach 1980, 1981), varies from 13–95; values falling within the range 10–100 are typical of many modern geothermal

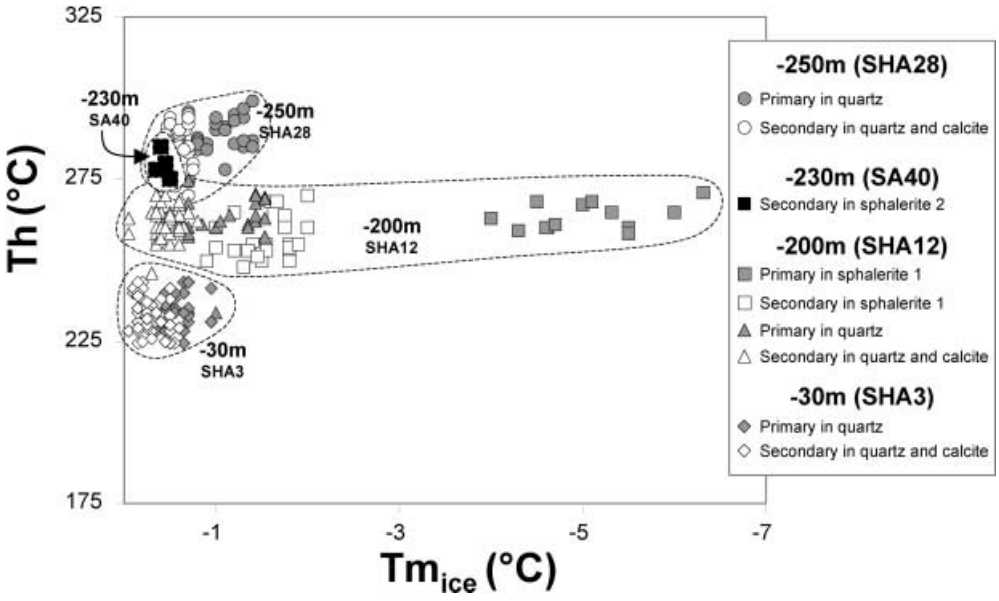

Fig. 7 Homogenization temperatures versus melting temperature of ice for the four structural levels studied in the Apacheta deposit (–250 m, SHA 28; –230 m, SA 40; –200 m, SHA 12; –30 m, SHA 3). In each level, distinctions are made for the nature of mineral hosting the fluid inclusions and for occurrence as primary or secondary inclusion

systems (Hedenquist and Henley 1985b). No temporal evolution can be described for this fluid, which was only observed in stage 2 of the paragenetic sequence.

In epithermal deposits, CO_2 is rarely observed as a liquid phase in fluid inclusions and its presence is usually only indicated by the presence of clathrate. The presence of liquid CO_2 in these Vw-c inclusions is unusual, even if such inclusions have already been observed in low-sulfidation deposits (McInnes et al. 1990; Van Leeuwen et al. 1990; McEwan et al. 1996).

Discussion and conclusions

Boiling and mixing appear as the most efficient of many processes that can lead to the deposition of ore and gangue minerals in an epithermal system. They effectively control compositional changes such as pH and the mineral solubilities of hydrothermal fluids in open channels during the last 1–2 km of ascent, thus constraining mineral deposition. This assumption is corroborated by direct observations of geothermal wells (Simmons and Browne 2000), the geochemistry of metal complexes (Seward 1973; Giggenbach and Stewart 1982; Gammons and Barnes 1989), and numerical modeling (Drummond 1981; Reed and Spycher 1984, 1985; Drummond and Ohmoto 1985; Seward 1989; Spycher and Reed 1989). Simple cooling of hydrothermal fluids (Drummond and Ohmoto 1985), dilution by cold groundwater (Spycher and Reed 1989; Hedenquist 1991), or interaction with surrounding wall rock (Spycher and Reed 1989) seem to be of less importance in governing ore deposition.

In the Apacheta deposit, boiling of an ascending Au–Ag-bearing hydrothermal fluid is proposed to explain the vertical changes in physico-chemical parameters of hydrothermal fluids, and thus the zonation and vertical extent of the resulting mineralization.

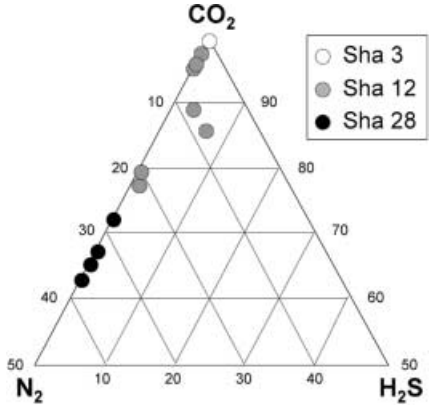

Fig. 8 Ternary CO_2-H_2S-N_2 diagram showing composition of the gaseous phase for the Vw-c fluids at three depth levels (–250 m, SHA 28; –200 m, SHA 12; and –30 m, SHA 3)

Evidence of boiling

Mineralogical evidence

Studies of active geothermal systems (Browne and Ellis 1970; Browne 1978; Henley and Hedenquist 1986; Keith and Muffler 1978; Simmons and Christenson 1994) and thermodynamic studies (Drummond and Ohmoto 1985; Reed and Spycher 1985; Simmons and Browne 2000) have shown that the presence of adularia and platy calcite, commonly pseudomorphosed by quartz as is the case here (Fig. 3C), is a strong indicator for boiling. The release of CO_2 to the vapor phase during boiling leads to a pH increase in the solution, causing a shift from the illite stability domain to that of adularia, and the precipitation of calcite and adularia [Eqs. (1) and (2)].

$$Ca^{2+} + 2HCO_3^- = CaCO_3 + CO_{2(g)} + H_2O \quad (1)$$

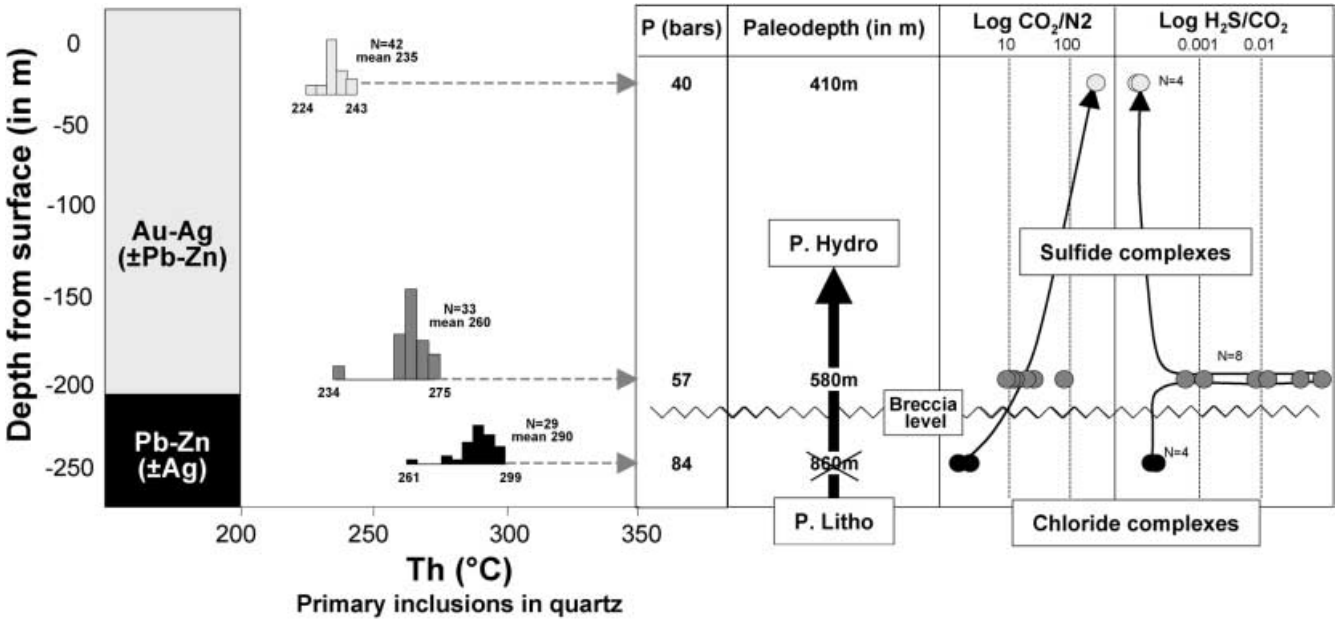

Fig. 9 Evolution of different parameters versus depth for SHA 28 (–250 m), SHA 12 (–200 m), and SHA 3 (–30 m) with from *left* to *right*: type of mineralization, homogenization temperature (*Th*), pressure and paleo-depth deduced from Th, and evolution of gas contents of the volatile phase of the Vw-c fluids with the logarithmic ratio of CO_2/N_2 and H_2S/CO_2

$$KAl_3Si_3O_{10}(OH)_2+6SiO_2+2HCO_3^-+2K^+ = 3KAlSi_3O_8+2CO_{2(g)}+2H_2O \quad (2)$$

Simmons and Browne (2000) show that platy calcite is restricted to a vertical zone near the site of first boiling. At Apacheta, platy calcite is mainly observed around the –250 to –200 m depth levels, which corresponds approximately to the maximum depth of precious-metal mineralization and suggests the proximity of first boiling.

Fluid evidence

Apart from mineralogical evidence, boiling is also demonstrated by direct fluid-inclusion studies. The presence of many fluid-inclusion planes containing only Vw-c inclusions of similar size and Rv ratio is a strong indicator of boiling as such filling cannot be linked to necking-down phenomena (Bodnar et al. 1985). Moreover, the coexistence of liquid-rich (Lw-c) and vapor-rich (Vw-c) primary and secondary inclusions in quartz from stage 2 suggests that boiling is not restricted to this stage, but occurs repeatedly during vein formation and probably during the main mineral-deposition stage 3.

The vertical trend of the Th-Tm diagram (Fig. 10) also suggests boiling (Hedenquist and Henley 1985b; Simeone and Simmons 1999). During the boiling of a gas-rich fluid, a small temperature drop involves a high CO_2 loss. The rapid loss of CO_2, contributing strongly to the apparent salinity (Bozzo et al. 1973; Collins 1979; Ramboz 1980; Hedenquist and Henley 1985a), implies a near-vertical trend in the Tm-value evolution (Hedenquist and Henley 1985b). Indeed, the vertical pattern of the Tm-Th diagram in each sample at different depths (black arrow in Fig. 10) strongly suggests a progressive boiling of the fluid with gas loss, implying a gas-rich parent fluid of unknown composition. The

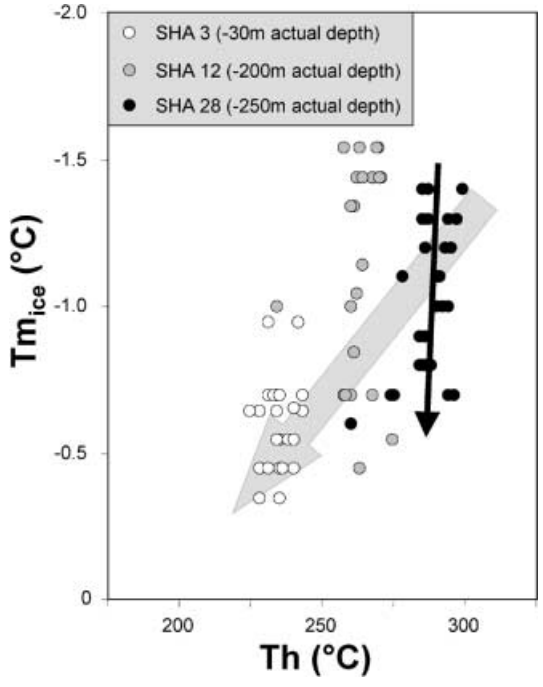

Fig. 10 Evolution of Tm_{ice} and Th for the Lw-c primary inclusions for three depth levels. *Black arrow* shows the evolution within a depth level, whereas *grey arrow* represents the global evolution of fluids with depth

more widely spaced Tm values for sample SHA 12 (–200 m actual depth) may indicate a zone of more intense boiling.

Figure 9 shows the variation of different gas ratios with depth for Vw-c inclusions. The continuous increase of the CO_2/N_2 ratio towards the surface is commensurate with the loss of N_2 in the deeper levels. The H_2S/CO_2 ratio is highest at the –200 m level; this gas content variation can also be a sensitive indicator of boiling, since the volatiles are fractionated into the vapor phase according to their solubility (Giggenbach 1980; Henley et al. 1984). H_2S is the most soluble in liquid water, followed by CO_2, CH_4, and N_2 (Giggenbach 1980; Drummond 1981; Drummond and Ohmoto 1985), and during boiling the ratio between gases will change. The evolution of different gas ratios with varying depth (Fig. 9) is also consistent with the boiling origin of such Vw-c fluids. The strong H_2S enrichment observed at –200 m (sample SHA 12) may indicate a level of intense liquid-vapor separation, corroborating the more widely spread Tm values (Fig. 10) and the fact that platy calcite is found at this same level.

Environment of mineralization

Temperature

In view of the shallow formation depth of epithermal deposits and the evidence of boiling, the temperature corrections due to pressure are negligible and the trapping temperatures of the hydrothermal fluids can be considered as roughly similar to the homogenization temperatures. The temperature conditions, given by both the Lw-c and Vw-c fluids, are thus constrained between 235 and 300 °C, with a decreasing temperature from the deepest sample (–250 m actual depth) to the shallowest sample (–30 m actual depth) (Fig. 9). This upward temperature decrease reflects a steep thermal gradient in the near-surface environment.

A gas geothermometer (Giggenbach 1981) was used to confirm the equilibration temperature of the hydrothermal fluid at depth. For Giggenbach, the reactions involving the breakdown of plagioclase to clay, calcite, pyrite, and chlorite exert a temperature-dependent control on the CO_2/H_2S ratio in a geothermal system. The temperature can also be calculated by the formula:

$$\mathrm{Tcs} = -6,630/\left[\log\left(X_{CO_2}/X_{H_2S}\right) - 14.1\right] \quad (3)$$

where X_{CO_2} and X_{H_2S} are the mole fractions of CO_2 and H_2S, and Tcs is the fluid temperature in degrees Kelvin.

The Tcs will vary with boiling since the gas ratios will vary. However, such effects are partially offset by the comparable solubility of these two gases and the logarithmic term of the gas ratio (Hedenquist et al. 1992). Application of this geothermometer to several H_2S-rich Vw-c inclusions of level 5,050 m gives temperatures in good agreement with the measured Th (Table 5) as well as agreeing with similar values for aqueous Lw-c fluids at the same depth level. As shown by Sherlock et al. (1995), this implies that the Tcs geothermometer is an efficient tool even in a boiling system.

Pressure conditions

Pressure conditions were estimated with the Lw-c fluid inclusions. The total fluid pressure is a function of the vapor pressure of water and the partial pressure of gas, since dissolved gases contribute to the total vapor pressure of the system (Hedenquist and Henley 1985b; Hedenquist et al. 1992; Barton and Chou 1993). Raman spectroscopy detected only CO_2 in the Lw-c inclusions, and the fact that no clathrates are observed by microthermometry indicates that the CO_2 content is below 3.7 wt% (Hedenquist and Henley 1985b). The maximum contribution pressure of the gases is thus equivalent to 10.4 bars.

Based on this maximum value for the CO_2 contribution pressure, using the boiling curves provided by Haas (1971) and assuming a 2 wt% NaCl fluid, the maximum hydrostatic fluid pressures in this hydrothermal system were 84, 57, and 40 bars for, respectively, present-day depth levels –250 m (SHA 28, average Th: 290 °C), –200 m (SHA 12; average Th: 260 °C), and –30 m (SHA 3; average Th: 235 °C).

Representative isochores have been drawn for the Vw-c fluids using equations of state from Bowers and Helgeson (1983), modified by Bakker (1999). However, the lack of some microthermometric data (Tm_{ice}, Tf_c, Th_{CO_2}), combined with the high vapor content and low density of the volatile phase ($Th_{CO_2} < 6$ °C) of the inclusions, requires some approximations in estimating the global composition of the inclusions, thus leading to more uncertainty for the pressure calculation than is acceptable.

Paleo-depth estimates

Using the hydrostatic fluid pressures obtained above and considering a hydrostatic pressure, we obtain estimated paleo-depths of –860, –580, and –410 m below the paleo-water table for the three samples. The calculated difference in paleo-depth between the two highest levels

Table 5 Temperatures (in °C) given by the Tcs geothermometer (Giggenbach 1981) applied to several Vw-c fluid inclusions in the H_2S-rich level (5,050 m, sample SHA 12, –200 m actual depth)

CO_2	H_2S	$\mathrm{Log}(CO_2/H_2S)$	Tcs (°C)	Th
97.7	1.03	1.9899	274	253
85.5	6.70	1.1059	237	280
88.9	3.30	1.4304	250	278
95.7	0.7	2.1358	281	?

(580–410 m = 170 m) agrees with the actual position of these two samples in the mine (200–30 m = 170 m), even though the studied samples SHA 3 and SHA 12 are not from the same vein. Once again, it validates the assumption based on mineralogical work suggesting identical mineralizing processes for most of the Apacheta veins (see above).

However, the estimated paleo-depth for the deepest sample SHA 28 disagrees with its actual depth (860 m, instead of the 630 m expected from the actual spatial relationship of these three samples in the mine) (Fig. 9). Three hypotheses can be proposed for explaining this difference in height: (1) a later fault has affected the mineralized system, with down-throw of the bottom of the column that displaced the sample sites relative to each other; (2) a local fluid overpressure has lead to an erroneous and over-evaluated depth value; and/or (3) a change has occurred in the pressure regime between the top and bottom of the mineralized column, from lithostatic to hydrostatic fluid pressure during the mineralizing event. Based on our field experience and fluid knowledge, the preferred interpretation for explaining this 230-m height discrepancy is this last hypothesis of a change in the pressure regime. Abundant hydrothermal breccias, observed between 220 and 240 m actual depth (Fig. 9), may express this change of pressure regime from lithostatic to hydrostatic conditions.

Boiling and mineralizing processes

In most epithermal settings, gold and silver are most efficiently transported as bisulfide complexes (Seward 1973, 1989; Romberger 1988; Shenberger and Barnes 1989; Hayashi and Ohmoto 1991), whereas base metals are transported mainly as chloride complexes (Seward 1973; Henley et al. 1984; Gammons and Barnes 1989).

When boiling occurs in the deeper part of the system, the pH will first increase due to CO_2 loss [Eq. (1)], leading to the destruction of chloride complexes and the precipitation of base-metal sulfides [Eq. (4); Drummond and Ohmoto 1985; Cole and Drummond 1986]:

$$MeCl_2(aq) + H_2S(aq) = MeS + 2H^+ + 2Cl^- \quad (4)$$

However, the first boiling cannot be the prime cause of gold precipitation, because gold solubility initially increases during this deep boiling (Fig. 11) due to the pH and f_{O2} increases. H_2S, more soluble than CO_2 and N_2, is lost proportionally less than CO_2. The first net effect of boiling is thus a slight increase in gold solubility (Fig. 11; Brown 1989; Seward 1989). Only when the loss of H_2S in the vapor phase becomes dominant over the pH increase will gold precipitate. Gold deposition thus occurs mainly in response to boiling through the loss of H_2S in the vapor phase and a drop in temperature [Eq. (5); Brown 1989; Seward 1989; Hedenquist 1996; Simmons and Browne 2000]:

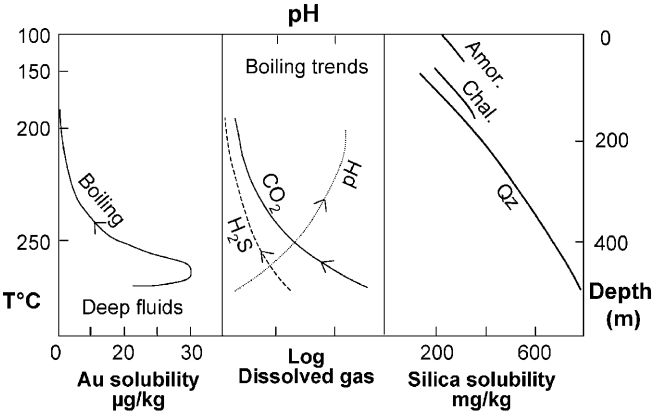

Fig. 11 Evolution of Au solubility, dissolved gas, and silica solubility as a function of temperature and depth in geothermal areas. Initial boiling and CO_2 loss cause a pH increase, which increases Au solubility as a bisulfide complex. However, in the end the loss of H_2S, the main Au ligand, overcomes the pH increase, causing a rapid decrease in Au solubility and thus gold deposition (Brown 1986)

$$Au(HS)_2^- + \tfrac{1}{2}H_{2(g)} = Au + HS^- + H_2S_{(g)} \quad (5)$$

During a similar boiling event, sulfur-complexed species will precipitate paragenetically later than chloride-complexed sulfides, due to the slower loss of sulfur to the vapor phase and the resulting decrease in sulfur fugacity of the solution.

The variation in gas composition due to the differential fractionation of volatiles during boiling accounts for the observed metal zoning in the Shila Apacheta deposit. Phase separation (boiling) may start in the deepest part of the system at about 250 m actual depth. Overpressure at 200 m actual depth may occur, resulting in rupture and hydrothermal brecciation. Rupture, accompanied by a rapid drop in pressure, causes a hydrothermal eruption and a catastrophic liquid-vapor phase separation involving a very rapid and total loss of volatiles from the liquid to the vapor phase. The high H_2S content of the vapor inclusions at the –200 m level (Figs. 8 and 9) corroborates its depletion in the liquid phase; this depletion will decrease the solubility of precious metals, which then can precipitate downstream in the (ascending) fluids. The precious-metal mineralization observed above –200 m actual depth at Shila Apacheta is thus linked to physical and chemical changes in the hydrothermal fluid, associated with liquid-vapor separation in an upward boiling front.

Acknowledgements This research is part of doctoral studies by the senior author and has been carried out within the framework of the French Metallogeny GdR research programme (Gold theme). Thanks are due to Cedimin S.A. for its financial and field support, and to J. Dubessy, M.C. Boiron, and T. Lhomme for the Raman analyses. M.L. Silberman, M. Cardozo, and B. Lehmann are thanked for their constructive reviews which significantly improved this paper. H.M. Kluijver edited the English version of this paper.

References

Bakker RJ (1999) Adaptation of the Bowers and Helgeson (1983) equation of state to the H_2O–CO_2–CH_4–N_2–NaCl system. Chem Geol 154:225–236

Barton PB, Chou I (1993) Refinement of the evaluation of the role of CO_2 in modifying estimates of the pressure of epithermal mineralization. Econ Geol 88:873–884

Berger BR, Eimon P (1983) Conceptual models of epithermal precious metal deposits. In: Shanks WC III (ed) Cameron volume on unconventional mineral deposits. Australasian Institute of Mining and Metallurgy, pp 191–205

Bodnar RJ (1993) Revised equation and table for determining the freezing point depression of H_2O–NaCl solutions. Geochim Cosmochim Acta 57:683–684

Bodnar RJ, Reynolds TJ, Kuehn CA (1985) Fluid inclusion systematics in epithermal systems. In: Berger BR, Bethke PM (eds) Geology and geochemistry of epithermal systems. Rev Econ Geol 2:73–97

Boiron MC, Essaraj S, Sellier E, Cathelineau M, Lespinasse M, Poty B (1992) Identification of fluid inclusions in relation to their host microstructural domains in quartz by cathodoluminescence. Geochim Cosmochim Acta 56:175–185

Bowers TS, Helgeson HC (1983) Calculation of the thermodynamic and geochemical consequences of nonideal mixing in the system H_2O–CO_2–NaCl on phase relations in geologic systems: equation of state for H_2O–CO_2–NaCl fluids at high pressures and temperatures. Geochim Cosmochim Acta 47:1247–1275

Bozzo AT, Chen HS, Kass JR, Barduhn AJ (1973) The properties of the hydrates of chlorine and carbon dioxide. In: Proc 4th Int Symp on Fresh Water from the Sea, Rep 3, pp 437–451

Brown KL (1986) Gold deposition from geothermal discharges in New Zealand. Econ Geol 81:979–983

Brown KL (1989) Kinetics of gold precipitation from experimental hydrogen sulfide solutions. Econ Geol Monogr 6:320–327

Browne PRL (1978) Hydrothermal alteration in active geothermal fields. Annu Rev Earth Planet Sci 6:229–250

Browne PRL, Ellis AJ (1970) The Ohaki-Broadlands hydrothermal area, New Zealand: mineralogy and related geochemistry. Am J Sci 269:97–131

Buchanan LJ (1981) Precious metal deposits associated with volcanic environments in southwest Arizona. Ariz Geol Soc Dig 14:237–262

Candiotti de Los Rios H, Noble DC, McKee EH (1990) Geologic setting and epithermal silver veins of the Arcata District, southern Peru. Econ Geol 85:1473–1490

Cassard D, Chauvet A, Bailly L, Llosa F, Rosas J, Marcoux E, Lerouge C (2000) Structural control and K/Ar dating of the Au-Ag epithermal veins in the Shila Cordillera, southern Peru. C R Acad Sci Paris 330:23–30

Chauvet A, Cassard D, Bailly L (1999) Process of formation of the Au-Ag Shila-Paula epithermal vein system (southern Peru). In: Proc Int Symp on Andean Geodynamics, Göttingen, pp 159–162

Clarke DS, Govett GJS (1990) Southwest Pacific epithermal gold: a rock-geochemistry perspective. J Geochem Explor 35:225–240

Cole DR, Drummond SE (1986) The effect of transport and boiling on Ag/Au ratios in hydrothermal solutions: a preliminary assessment and possible implications for the formation of epithermal precious-metal ore deposits. J Geochem Explor 25: 45–79

Collins PLF (1979) Gas hydrates in CO_2 bearing fluid inclusions and the use of freezing data for estimation of salinity. Econ Geol 74:1435–1444

Drummond E, Ohmoto H (1985) Chemical evolution and mineral deposition in boiling hydrothermal systems. Econ Geol 80: 126–147

Drummond SE (1981) Boiling and mixing of hydrothermal fluids. PhD Thesis, Pennsylvania State University, 380 pp

Dubessy J, Guilhaumou N, Mullis J, Pagel M (1984) Reconnaissance par microspectrometrie Raman, dans les inclusions fluides, de H_2S et CO_2 solides à domaine de fusion comparable. Bull Min 107:189–192

Ewers GR, Keays RR (1977) Volatile and precious metal zoning in the Broadlands geothermal field, New Zealand. Econ Geol 72:1337–1354

Gammons CH, Barnes HL (1989) The solubility of Ag_2S in near-neutral aqueous solutions at 25 to 300 °C. Geochim Cosmochim Acta 53:279–290

Gibson PC, Noble DC, Larson LT (1990) Multistage evolution of the Calera epithermal Ag-Au vein system, Orcopampa District, southern Peru: first results. Econ Geol 85:1504–1519

Gibson PC, McKee EH, Noble DC, Swanson KE (1995) Timing and interrelation of magmatic, tectonic and hydrothermal activity at the Orcopampa district, southern Peru. Econ Geol 90:2317–2325

Giggenbach WF (1980) Geothermal gas equilibria. Geochim Cosmochim Acta 44:2021–2032

Giggenbach WF (1981) Geothermal mineral equilibria. Geochim Cosmochim Acta 45:393–410

Giggenbach WF, Stewart MK (1982) Processes controlling the isotopic composition of steam and water discharges from steam vents and steam-heated pools in geothermal areas. Geothermics 11:71–80

Haas JL (1971) The effect of salinity on the maximum thermal gradient of a hydrothermal system at hydrostatic pressure. Econ Geol 66:940–946

Hayashi K, Ohmoto H (1991) Solubility of gold in NaCl- and H_2S-bearing aqueous solutions at 250–350 °C. Geochim Cosmochim Acta 55:2111–2126

Hedenquist JW (1991) Boiling and dilution in the shallow portion of the Waiotapu geothermal system, New Zealand. Geochim Cosmochim Acta 55:2753–2765

Hedenquist JW (1996) Hydrothermal systems in volcanic arcs. In: Origin of and exploration for epithermal gold deposits, Short course, 22–23 April, Geneva, 139 pp

Hedenquist JW, Henley RW (1985a) Hydrothermal eruptions in the Waiotapu geothermal system, New Zealand. Econ Geol 80:1640–1668

Hedenquist JW, Henley RW (1985b) The importance of CO_2 on freezing point measurements of fluid inclusions: evidence from active geothermal systems and implications for epithermal ore deposition. Econ Geol 80:1379–1406

Hedenquist JW, Reyes AG, Simmons SF, Taguchi S (1992) The thermal and geochemical structure of geothermal and epithermal systems: a framework for interpreting fluid inclusion data. Eur J Mineral 4:989–1015

Henley RW, Ellis AJ (1983) Geothermal systems, ancient and modern. Earth Sci Rev 19:1–50

Henley RW, Hedenquist JW (1986) Introduction to the geochemistry of active and fossil geothermal systems. In: Henley RW, Hedenquist JW, Roberts PJ (eds) Guide to the active epithermal systems and precious metal deposits of New Zealand. Monogr Series Mineral Deposits 26: 129–145

Henley RW, Truesdell AH, Barton PB Jr, Whitney JA (eds) (1984) Fluid mineral equilibria in hydrothermal systems. Rev Econ Geol 1

Hollister, Silberman ML (1995) The age of gold-silver-precious metals at Bodie. Ariz Geol Soc Dig 22:297–305

Jannas R (1998) Resumen consultario Proyecto Chipmo. Buenaventura SA, Lima

Keith TEC, Muffler LPJ (1978) Minerals produced during cooling and hydrothermal alteration of ash flow tuff from Yellowstone drill holeY-5. J Volc Geotherm Res 3:373–402

McEwan CJA, Fallick AE, Rice CM (1996) The Rosita Hills epithermal Ag-base metal deposits, Colorado, USA. A stable and fluid inclusion study. Miner Deposita 31:41–51

McInnes BIA, Crocket JH, Goodfellow WD (1990) The Laforma deposit, an atypical epithermal-Au system at Freegold Mountain, Yukon Territory, Canada. J Geochem Explor 36:73–102

Petersen PS, Noble DC, McKee EH, Eyzaguirre VR (1983) A resurgent mineralized caldera in southern Peru. EOS Trans Am Geophys Union 64:884

Petersen U, Vidal CE, Noble DC (1990) Tetrahedrite compositional zoning and ore distribution in the Orcopampa vein system, Orcopampa, Peru. Econ Geol 85:1287–1302

Pirajno F (1992) Hydrothermal mineral deposits. Principles and fundamental concepts for the exploration geologist. Springer, Berlin Heidelberg New York

Poty B, Leroy J, Jachimowicz L (1976) Un nouvel appareil pour la mesure des temperatures sous le microscope, l'installation de microthermométrie Chaix-Meca. Bull Soc Fr Min Cristallogr 99:182–186

Ramboz C (1980) Problèmes posés par la détermination de la composition des fluides carboniques complexes, à l'aide des techniques microthermométriques. C R Acad Sci Paris 290: 499–502

Reed MH, Spycher NF (1984) Calculation of high temperature pH and mineral equilibria in hydrothermal waters, with application to geothermometry and studies of boiling and dilution. Geochim Cosmochim Acta 48:1479–1492

Reed MH, Spycher NF (1985) Boiling, cooling and oxidation in epithermal systems: a numerical modeling approach. Rev Econ Geol 2:249–272

Roedder E (1984) Fluid inclusions. Rev Mineral 12:1–644

Romberger SB (1988) Geochemistry of gold in hydrothermal deposits. US Geol Surv Bull 1857A:A9–A25

Seward TM (1973) Thio complexes of gold and the transport of gold in hydrothermal ore solutions. Geochim Cosmochim Acta 37:379–399

Seward TM (1989) The hydrothermal chemistry of gold and its implications for ore formation: boiling and conductive cooling as examples. Econ Geol Monogr 6:394–404

Shenberger DM, Barnes HL (1989) Solubility of gold in aqueous sulfide solutions from 150 to 350 °C. Geochim Cosmochim Acta 53:269–278

Sherlock RL, Tosdal RM, Lehrman NJ, Graney JR, Losh S, Jowett EC, Kesler SE (1995) Origin of the McLaughlin mine sheeted vein complex: metal zoning, fluid inclusion, and isotopic evidence. Econ Geol 90:2156–2181

Silberman ML, Berger BR (1985) Relationship of trace element patterns to alteration and morphology in epithermal precious-metal deposits. Rev Econ Geol 2:203–232

Silberman ML, McKee EH, Noble DC (1985) Age of mineralization at the Cailloma and Orcopampa silver districts, southern Peru. Isochron/West 43:597–603

Simeone R, Simmons SF (1999) Mineralogical and fluid inclusions studies of low-sulfidation epithermal veins at Osilo (Sardinia), Italy. Miner Deposita 34:705–717

Simmons SF, Browne PRL (2000) Hydrothermal minerals and precious metals in the Broadlands-Ohaaki geothermal system: implications for understanding low-sulfidation epithermal environments. Econ Geol 95:971–999

Simmons SF, Christenson BW (1994) Origins of calcite in a boiling geothermal system. Am J Sci 294:361–400

Spycher NF, Reed MH (1989) Evolution of a Broadlands-type epithermal ore fluid along alternative P-T paths: implications for the transport and deposition of base, precious and volatile metals. Econ Geol 84:328–359

Van Leeuwen TM, Leach T, Hawke AA, Hawke MM (1990) The Kelian disseminated gold deposits, East Kalimantan, Indonesia. In: Hedenquist JW, White NC, Siddeley G (eds) Epithermal gold mineralization of the circum-Pacific: geology, geochemistry, origin and exploration, I. Elsevier, Amsterdam, pp 1–61